RESEARCH PAPER

Effect of Electrolytic Solution on Corrosion Behavior and Mechanical Properties of a Coated AZ31 Magnesium Alloy via Plasma Electrolytic Oxidation Process

Yasin Mehdizadeh[1], Saeed Reza Allahkaram[2,*], Majid Shamsarjmand[3], Mohammad H. Mohammad Ebrahimi[1]

* akaram@ut.ac.ir

[1] School of Metallurgy and Materials Engineering, College of Engineering, University of Tehran
[2] School of Metallurgy and Materials Engineering, College of Engineering, University of Tehran, P.O. Box 11155-4563, Tehran, Iran
[3] Department of Aerospace Engineering, Sharif University of Technology, Tehran, Iran

Abstract: The present work investigates the corrosion behaviour and mechanical properties of a coted AZ31 magnesium alloy through the plasma electrolyte oxidation (PEO) coating process in different alkaline electrolytes, specifically sodium silicate (Si-coating), sodium polyphosphate (P-coating), and sodium aluminate (Al-coating). Scanning electron microscopy (SEM) equipped with energy-dispersive X-ray spectroscopy (EDX) and x-ray diffraction was used to investigate the morphology, chemical composition, and phase structure of the coatings. Microscopic scrutiny revealed that the layer in the phosphate electrolyte was twice as thick and had a higher relative porosity percentage compared to those formed in the other electrolytes. The phase analysis indicated that MgO was the prevailing phase in both the Al-coating and P-coating. However, the dominant phase in the Si-coating was Mg_2SiO_4. Electrochemical testing was conducted in a solution containing 3.5 wt% sodium chloride, demonstrating improvements in the corrosion resistance of coated alloys. These investigations confirmed that the corrosion resistance of Si-coating was dramatically higher than that of others, which could be attributed to the presence of the dense and stable Mg_2SiO_4 phase as well as its relatively low porosity. According to the results of the tensile tests, the coated samples exhibited lower tensile strength and elongation compared to the uncoated ones. The tensile strength and elongation decreased when the electrolyte was changed from Al-coating to P-coating, while the yield strength remained almost unchanged. Further analyses indicated that the drop in tensile strength and elongation could be attributed to the presence of cracks and pores in the brittle PEO ceramic coating, which act as stress concentration regions during deformation. Those areas are created due to thermal stress during the coating process and deformation in the elastic stage.

Keywords: Mechanical properties, AZ31 magnesium alloy, Plasma electrolytic oxidation (PEO), Corrosion behavior.

1. INTRODUCTION

Magnesium alloys with special properties such as low density, high specific strength, excellent damping capacity, and good protection against electromagnetic waves have great potential in engineering applications, including the aerospace, automotive, and electronics industries. At the same time, there remains a concern about their poor corrosion resistance due to their high chemical activity and very negative electrochemical potential. The latter severely weakens the mechanical properties by creating stress concentration areas. For this reason, the use of magnesium alloys is limited [1, 2].

Various surface treatments have been introduced to improve the corrosion properties of magnesium alloys, including conversion coatings [3], electroplating [4], anodizing [5], plasma electrolytic oxidation [6], polymer coatings [7], and physical vapor deposition (PVD) [8]. The plasma electrolytic oxidation (PEO) process is recognized as a relatively new and cost-effective method for modifying the surface of valve metals (aluminum, titanium and magnesium) in environmentally friendly alkaline electrolytes through producing dense, hard, and adhesive ceramic coatings, which boosts the corrosion resistance of the substrate [9]. To improve the quality of the coating formed on magnesium alloys, knowledge of the mechanisms and parameters affecting the PEO process is essential [10]. Thus, many studies have been undertaken on the ignition mechanism and growth of the coating, as well as parameters affecting the quality of the coating, including electrolyte composition, electrical parameters of the device, and coating time [11-14]. In this regard, by examining the effect of SiO_3^{2-}, PO_4^{3-}, and AlO_2^{-}

anions on the corrosion properties of PEO coating applied to AM50 magnesium alloy, Ghasemi et al. [15] observed that these anions affect the coating characteristics such as thickness, chemical composition, and structure of the coating. They reported that the coating formed in the electrolyte containing SiO_3^{2-} showed more favorable corrosion properties than the two electrolytes due to its thickness, low open porosity, and optimal barrier layer resistance. Rahman et al. [16] also evaluated the effect of three additives of phosphate, silicate, and aluminate to electrolytes containing NaOH and Na_2SiF_6 on the structure and tribological characteristics of the coating. The results of this study revealed that the layer formed in the electrolyte containing alumina had better hardness and tribological properties.

In general, to improve the corrosion resistance of magnesium, various processes are used to prevent the loss of mechanical properties of the alloy. For example, extensive research has been done to explore the effect of plasma electrolytic oxidation treatment on the mechanical properties while specimens have been exposed to a corrosive environment, such as stress corrosion cracking behavior of magnesium alloy [17-19].

However, the important question that remains is what effect do such corrosion resistance-enhancing processes have on mechanical properties alone?

To date, no review has been conducted on the effect of the PEO process on these alloys before exposure to a corrosive atmosphere. This study aims to determine the effect of the coating process on the potential attenuation or strengthening of mechanical properties before the corrosion process takes effect, to assess whether the sample meets the necessary conditions for use in the relevant industry. The present study characterizes the corrosion behavior of oxide coatings formed by plasma electrolytic oxidation (PEO) method on the AZ31 magnesium alloy in three different electrolytes sodium polyphosphate, sodium silicate, and sodium aluminate. Then, the effect of this process on improving the mechanical properties of alloys was explored.

2. EXPERIMENTAL PROCEDURES

2.1. Preparation of Specimens, Electrolyte Solutions, and PEO Treatment

A wrought magnesium alloy of grade AZ31 with a nominal composition in Table 1 was employed in this investigation. Specimens measuring 26 mm × 26 mm × 5 mm were ground successively with 600, 800, 1000, and 2500 grit emery sheets and washed in acetone before the PEO treatment. The PEO process was carried out using a pulsed DC power source with a bipolar pulse of t_{on}:t_{off}= 55:15 (1000 Hz). This gradient pulse was repeated with a frequency of 1000 Hz. During the PEO process, a constant current setting was employed by a square pulse and anodic/cathodic pick ratio ($I_+/I_- = 1$) for 5 min. This wave was applied to magnesium alloy for 5 min at room temperature. AZ31 alloy specimens and stainless-steel plates, placed around the cell, were used as the anode and cathode, respectively. As reported in Table 2, the three electrolytes were prepared separately, using distilled water as the solvent. The electrolyte was continuously stirred using a magnetic stirrer during the coating process. The electrolyte temperature was kept constant at 23°C utilising a heat exchanger system. The potential discrepancies between the anode and the cathode were recorded instantly by a multimeter equipped with a Ziegler RM-232 data recorder. Finally, the coated samples were rinsed with deionized water and dried in warm air.

2.2. Characterization, Electrochemical, and Tribological Evaluations

The surface morphologies, thickness, and chemical composition of the PEO-AZ31 alloys were characterized using scanning electron microscopy (Cam Scan-MV2300).

Table 1. The chemical composition of AZ31 magnesium alloy

Elements	Al	Zn	Mn	Si	Cu	Ni	Fe	Other	Mg
(wt.%)	2.5-3.5	0.6-1.4	0.2-1.0	0.1	0.04	0.005	0.005	0.3	Balance

Table 2. Electrolyte composition and coating process parameter

Samples	Electrolyte composition (g/L)	Flow density ($\frac{A}{cm^2}$)	t_+/t_-	Frequency (Hz)
P-coating	10 g/L Na(PO$_3$)$_n$ + 4 g/L KOH			
Si-coating	10 g/L Na$_2$SiO$_3$ + 4 g/L KOH	0.2	$\frac{55}{15}$	1000
Al-coating	10 g/L NaAlO$_2$ + 4 g/L KOH			

For cross-sectional analysis of the PEO-AZ31 alloys, the alloys were mechanically cut in half using a wire cut. Cross-sections were prepared through hand polishing with 600–1200 grit SiC paper in succession.

All samples were coated with a thin layer of gold/palladium using a sputter coater (Bio-Rad E5400) to enhance conductivity and improve imaging using SEM. Elemental mapping was performed using an EDX (Bruker AXS5350, Germany). The porosity and coating thickness measurements were performed based on at least three SEM micrographs of each sample, using MIP plus Processing Lab image analysis software for assistance.

The XRD measurements were performed using a commercial X-ray diffractometer (Philips Xpert, λ= 1.5406 A, 40 mA, 40 kV). The scanning range of the diffraction angle (2θ) was set between 10° and 100° with a step size of 0.02° and a time step of 1 s. Due to the low thickness of the coating and its high porosity, the coatings were pulverised, after which an X-ray diffraction test was performed on them.

The electrochemical measurements were made on bare and PEO-coated AZ31 magnesium samples in 3.5 wt.% NaCl solution using a three-electrode system including a magnesium specimen as the working electrode, a graphite mesh as the auxiliary electrode, and a calomel electrode as the reference electrode.

A potentiodynamic polarisation test was carried out from a potential of -0.4 V (vs. OCP) to 1 V SCE with a scan rate of 1 mV/s. An electrochemical impedance spectroscopy (EIS) test was conducted on these specimens using a Potentiostat/Galvanostat (Solartron 1260 model) coupled with a frequency response analyser (FRA) at an open-circuit potential (OCP) in 3.5 wt.% NaCl electrolyte solution after 60 minutes of immersion at 25°C, along with sinusoidal perturbation equal to 5 mV from 100 kHz to 10 mHz frequency range. The impedance spectra were analyzed by ZsimpWin software.

The mechanical properties of the experimental alloy and processed materials were evaluated using the tensile testing method. The tensile specimens were prepared according to the E8 standard with a 20-mm gauge length, 3-mm gauge width, and 1-mm thickness. The room temperature tensile tests were carried out utilising an STM50 testing machine with a strain rate of 10^{-4} s^{-1}.

3. RESULTS AND DISCUSSION

3.1. Voltage-Time Response Curve of PEO Process

Fig. 1 displays the voltage-time curve of the PEO process in base electrolytes of silicate, phosphate, and aluminate for 300 seconds. The samples were coated at constant current density, consisting of two parts: ion current and electric current density [20].
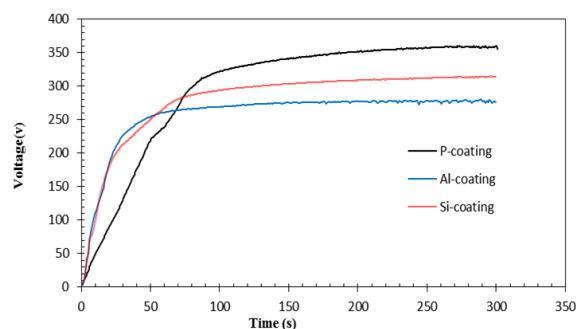

Fig. 1. Voltage-time response curves of the PEO-coated samples

These curves show three steps for all samples. In the first stage, the dissolution of the metal, caused by applying a voltage, was accompanied by the formation of a thin layer of oxide, followed by the release of oxygen gas through the normal anodising process. At this stage, the ionic fraction of the current density was dominant, and as a result, the voltage values increased due to the increase in ionic resistance because of the growth rate of the oxide film [20]. In the second stage, once the voltage reached a critical value (D-electric breakdown voltage), the voltage growth rate diminished and continued until a stable voltage was reached, which can be attributed to both ionic and electrical parts of the current density [21]. This stage began with tiny blue or white sparks, followed by yellow micro-sparks caused by micro-discharges. During the third stage, after reaching a stable voltage, the micro-sparks enlarged, their life increased, while the number of sparks decreased. The breakdown voltage, stabilisation voltage, and conductivity of the electrolyte for the Si-coating, Al-coating, and P-coating are summarised in Table 3. As can be seen, D-electric breakdown voltage and stability voltage are strongly dependent on the ion composition and conductivity of the electrolyte [22].

The relationship between the breakdown voltage and the ion conductivity of the electrolyte is

expressed through the theoretical model proposed in Eq. (1) by Ikonopisov [23]:

$$V_{BD} = a_B + b_B \log\frac{1}{k} \qquad (1)$$

Where V_{BD} represents the breakdown voltage, α_B denotes a definite constant for the metal, b_B is a definite constant for the electrolyte, and k shows the ionic conductivity of the electrolyte.

Considering the inverse relationship between the breakdown voltage and the ionic conductivity of the electrolyte, it can be concluded that the reduction of the ionic conductivity of the electrolytes from Si-coating, Al-coating, and P-coating, respectively, increased the breakdown voltage of their respective coatings.

3.2. Morphology and Chemical Composition of Coating

Surface morphology and image analysis of porosity of coatings are shown in Fig. 2.

Surface porosity is visible in all three coatings. Cavities and micro-cracks on the surface are caused by the release of oxygen gas and oxide melting due to the electrolysis process, local plasma temperature and pressure, and thermal stresses due to cooling of the oxide melt, respectively [24]. Researchers have argued that coating time and current density determine the quality of the coating [25, 26]. Meanwhile, the results of image analysis of porosities (Table 4) reveal that, at equal coating times and current densities for different electrolytes, the percentage of porosity and cavity diameter increase, leading to enhanced stability and breakdown voltages of the coating process.

Eq. (2) indicates the relationship between voltage and single pulse energy (E_P):

$$E_P = \int_0^{t_{on}} U_p \cdot I_p dt \qquad (2)$$

Where U_P is the pulse voltage, I_p denotes the pulse current, and t_{on} is the pulse-on time. According to this equation, as the voltage increases, so does the single pulse energy; thus, the morphological characteristics and growth rate of the coating are affected by the voltage and micro-discharge characteristics [27].

On the other hand, the breakdown voltage and other electrical characteristics of the process depend on the composition of the electrolyte.

Fig. 3 depicts the SEM micrograph and the distribution map of the elements at the cross-section of the samples. The thickness of PEO coatings depends on the electrical parameters and the time of the coating process [28]. Given that the current density and the time of coating had constant values, the thickness of the coatings had to be approximately equal; however, the stability voltage and, consequently, the pulse energy varied in different electrolytes. According to the values of the stability voltage reported in Table 3, it was expected that P-coating and Al-coating would have the highest and lowest thicknesses, respectively, as shown in Fig. 3 and Table 5. In coating growth rate calculations, the time to reach the breakdown voltage has been considered as the beginning of the coating growth phase. The elemental distribution map of P-coating clearly shows the presence of large cavities caused by large PEO sparks that have reached from the surface to near the interface of the coating and the substrate. For Si-coating, there are some holes in the middle of the coating.

Table 3. Process parameters in different electrolytes

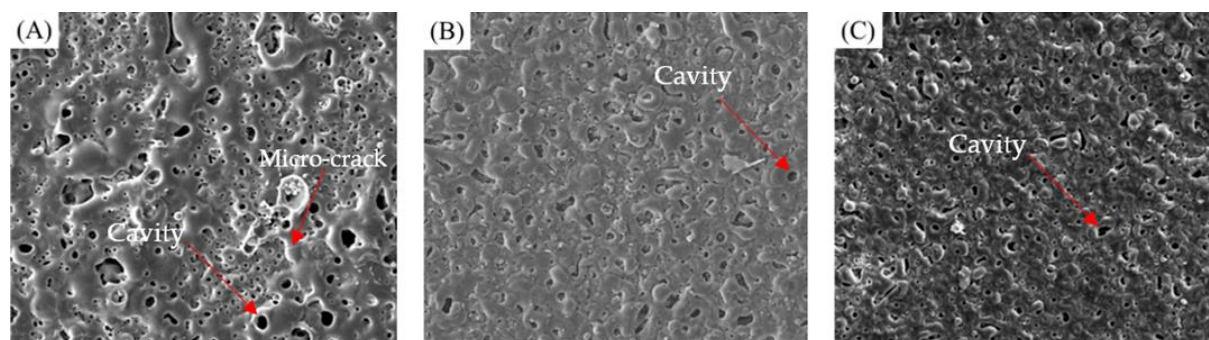| Samples	Conductivity of electrolyte (mS/cm)	V_{BD}	V_s
P-coating	14.7	220	360
Si-coating	18.3	185	315
Al-coating	21.5	180	280

Fig. 2. Surface morphology and image analysis of porosity A) P-coating, B) Si-coating, C) Al-coating

Table 4. Average pore diameter and porosity percentage for different electrolytes

Samples	Average pore diameter (µm) ± 0.1	Porosity percentage (%) ± 0.2
P-coating	1.5	5.7
Si-coating	1.3	4.3
Al-coating	0.7	3.6
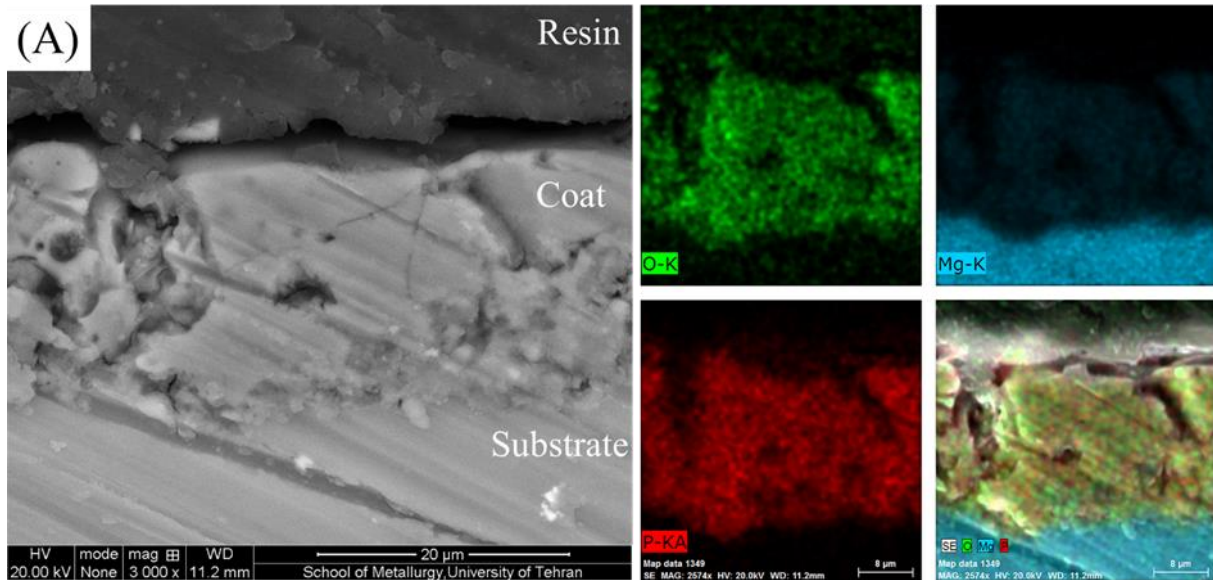
Fig. 3. Cross section SEM micrographs and elemental distribution map of a) P-coating, b) Si-coating, c) Al-coating.

Table 5. Average coating thickness for coatings produced in three different electrolytes

Samples	Average coating thickness (µm) ± 0.1	Coating growth rate (µm/min)
P-coating	19.6	4.9
Si-coating	12.2	2.6
Al-coating	7.3	1.6

The elemental distribution map of the Al-coating, despite its uniformity in growth, reveals discontinuities and low compression in the inner part of the coating. As can be seen in the Al element distribution map for the Al-coating, only on the surface of the coating are more stable compounds with suitable compaction of aluminate anions and substrate metal cations formed.

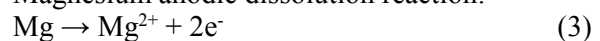### 3.3. Phase Composition of Coating

Fig. 4 demonstrates the XRD pattern of Si-coating, P-coating, and Al-coating.

Phase composition, the thickness, and porosity of the coating are the effective parameters on the corrosion resistance performance of PEO coatings [5, 29]. The MgO and Mg phases are observed in all three samples. The presence of the Mg peak in the sample pattern is due to chips being removed from the substrate during the scraping of the coating. In addition to the MgO phase, $Mg_2P_2O_7$, $Mg_2SiO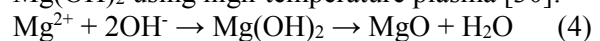_4$, and $MgAl_2O_4$ phases were also identified in the pattern depending on the type of electrolyte. The MgO phase has been predominant in P-coating and Al-coating, while the Mg_2SiO_4 phase has been predominant in the Si-coating.

The components of the electrolyte, such as Na_2SiO_3, $Na(PO_3)_n$, and ionised $NaAlO_2$, as well as OH^-, O_2^-, PO_3^-, SiO_3^{2-}, and AlO_2^{2-} anions, are produced through plasma electrolysis of the electrolyte at high voltages. Mg^{2+} cations are produced from the substrate atoms through discharge channels. The cation Mg^{2+} moves outwards while the mentioned anions move inwards in the path of the discharge channels to form a coating due to the strong electric field caused by the plasma, through performing chemical reactions:
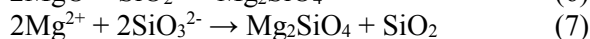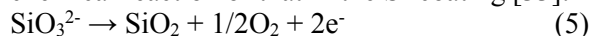
Magnesium anodic dissolution reaction:
$$Mg \rightarrow Mg^{2+} + 2e^- \qquad (3)$$
MgO formation reaction due to dehydration of $Mg(OH)_2$ using high-temperature plasma [30]:
$$Mg^{2+} + 2OH^- \rightarrow Mg(OH)_2 \rightarrow MgO + H_2O \qquad (4)$$
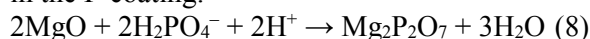Mg_2SiO_4 phase formation reactions at high-

90

temperature plasma [31, 32] and the formation chemical reaction of that in the Si-coating [33]:

$$SiO_3^{2-} \rightarrow SiO_2 + 1/2O_2 + 2e^- \quad (5)$$
$$2MgO + SiO_2 \rightarrow Mg_2SiO_4 \quad (6)$$
$$2Mg^{2+} + 2SiO_3^{2-} \rightarrow Mg_2SiO_4 + SiO_2 \quad (7)$$

The reaction of formation of the $Mg_2P_2O_7$ phase in the P-coating:

$$2MgO + 2H_2PO_4^- + 2H^+ \rightarrow Mg_2P_2O_7 + 3H_2O \quad (8)$$

The reaction of formation of $MgAl_2O_4$ phase in the Al-coating [2]:

$$AlO_2^- + 2H_2O \rightarrow Al(OH)_4^- \quad (9)$$
$$4Al(OH)_4^- - 4e^- \rightarrow 4Al(OH)_3 + 2H_2O + O_2 \quad (10)$$
$$2Al(OH)_3 \rightarrow Al_2O_3 + 3H_2O \quad (11)$$
$$Mg^{2+} + 2Al(OH)_4^- \rightarrow MgAl_2O_4 + 4H_2O \quad (12)$$
$$Al_2O_3 + MgO \rightarrow MgAl_2O_4 \quad (13)$$
$$Mg^{2+} + Al_2O_3 + 2OH^- \rightarrow MgAl_2O_4 + H_2O \quad (14)$$
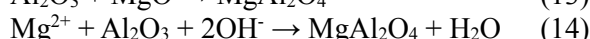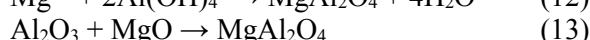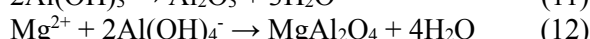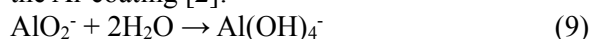$$AlO_2^- + Mg^{2+} \rightarrow MgAl_2O_4 \quad (15)$$
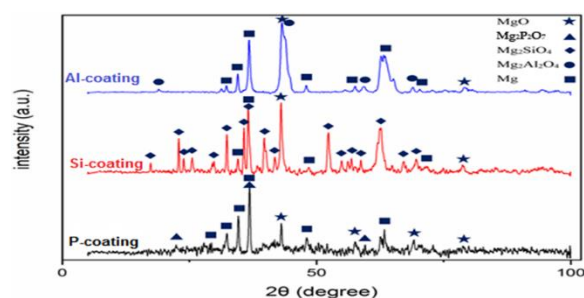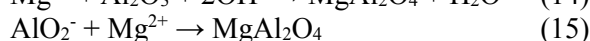
Fig. 4. XRD patterns for PEO-coated samples

3.4. Corrosion behavior

The corrosion behavior of the coatings was evaluated using polarization and electrochemical impedance methods compared to the open-circuit potential after one hour of immersion in 3.5 wt.% NaCl solution. Fig. 5 shows the changes in open-circuit potential over time. The choice of one-hour immersion time for the samples was to ensure that the coatings would reach a stable electrochemical condition.
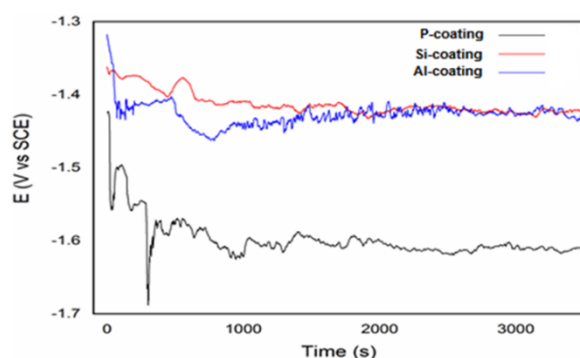

Fig. 5. Variation of open circuit potential (OCP) with time of PEO coated

Fig. 6 illustrates the Potentiodynamic polarization curves of samples coated in different electrolytes.
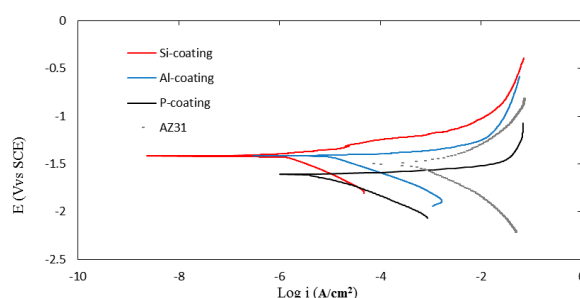

Fig. 6. Potentiodynamic polarization curves of PEO coated and bare Mg alloys at a scan rate of 0.25 mV/s in 3.5 wt.% NaCl solution

The apparent similarity of the curve of the coated samples can be related to the oxidative nature of the coatings; however, differences in test parameters such as corrosion current density (i_{corr}), corrosion potential (E_{corr}), as well as cathodic (β_c) and anodic (β_a) Tafel slopes can be attributed to differences in surface morphology and fuzzy compositions of the coatings. These parameters were extracted from potentiodynamic polarization curves using the ASTM G3 standard and the Tafel extrapolation method. The intersection of the two Tafel branches clarifies the corrosion procedure.

The corrosion potential (E_{corr}) is associated with the thermodynamic aspect, indicating the corrosion susceptibility, while the corrosion current density (i_{corr}) clarifies the average corrosion rate across the sampled surface [34]. The Stern-Geary also calculated the values of polarization resistance [35] relationship (Eq. 16) and presented them in Table 6.

$$R_p = \frac{\beta_\alpha \cdot |\beta_c|}{(2.303 I_{Corr}(\beta_\alpha + |\beta_c|))} \quad (16)$$

In general, a lower i_{corr}, a higher R_p, and a higher E_{corr} typically show a higher corrosion resistance and also a better coating corrosion resistance function [34, 36]. The resistance polarization of Al-coating, Si-coating, and P-coating increased by 3, 146, and 10 times compared to the reference sample (AZ31), respectively. The thickness and porosity are the two main factors affecting the corrosion resistance of coatings [37]. Al-coating has low corrosion resistance despite low surface porosity. As can be seen from the microscopic image and the elemental distribution map, the inner magnesium oxide layer lacks high corrosion resistance due to its low Pilling-Bedworth ratio (0.81) and poor continuity of the inner coating layer.

Table 6. Summary of DC polarization results for AZ31 substrate and PEO coated samples

Samples	I_{corr} $1*10^{-6}$ ± (A/cm^2)	E_{corr} (V)	β_C (V/dec)	β_α (V/dec)	R_p (kΩ.cm^2)
P-coating	9.8	-1.63	-0.14	0.05	3.2
Si-coating	1.1	-1.41	-0.19	0.07	43.8
Al-coating	27	-1.42	-0.17	0.02	1
AZ31	445	-1.52	-0.23	0.12	0.3

Despite the higher thickness of the P-coating compared to other samples, the high surface porosity and large pore diameter allow corrosive electrolyte penetration paths to the metal surface of the substrate; thus, the corrosion resistance of the P-coating is lower than that of the Si-coating. Fig. 7 shows the correlation between the i$_{corr}$ values of coated samples and electrical process characteristics, and morphological characteristics [38]. As can be seen from Fig. 7, the corrosion rate of coatings has no clear relationship with the morphological characteristics and variable electrical parameters of the coating process. Instead, the morphological characteristics of the coating are directly related to the stability voltage and break-down voltage, and are inversely associated with the electrical conductivity of the electrolyte. It can also be concluded that the corrosion behaviour of coatings does not depend solely on the morphological quality of the coating and may also be influenced by other parameters. The phenomenon that causes a significant difference in the corrosion resistance of the Si-coating from the other two coatings was probably related to two different factors. The first difference was the dominant phase formed in the Si-coating, which differed from the dominant phase in the other two coatings. The second difference was the quality of the inner layer of the coating, which could be better investigated using EIS. In Si-coating, according to the XRD results, spinel frostite phase (Mg$_2$SiO$_4$) was formed, which, according to previous studies, was much more compact and stable than the magnesium oxide phase (MgO) formed in the other two samples [5, 15-18, 20-33, 35, 37, 39].

Fig. 8 and Fig. 9 display the Nyquist and the Bode-phase curves of the P-coating, Si-coating, Al-coating, and AZ31 samples, respectively.

The impedance modulus obtained from the low-frequency Bode spectra, which are equivalent to the DC (polarization) test conditions, indicates that the Si-coating has 18 kΩ.cm^2. Polarisation resistance exhibits the best corrosion behaviour compared to the P-coating, Al-coating, and AZ31

sample, with values of 9.1, 2.4, and 0.9 kω, respectively cm^2 Polarization resistances, which are also consistent with the results of potentio-dynamic polarization curves. The Nyquist and Bode-phase plots of the AZ31 sample indicate that its equivalent circle (Fig. 10a) has a time constant corresponding to the electrolyte-substrate interface. The impedance spectra of Si-coating reveal two-time constants due to the two-layer coating structure; thus, the equivalent electrical circle (Fig. 10b) has also two time constants (RC). The low frequency time constant is related to the inner compact layer, while the high frequency time constant is related to the PEO coating [40]. A negative induction loop can be seen at the lower frequencies of the Nyquist curve of the Al-coating, which corresponds to an inductor element (L) and an inductive resistor (RL) in the equivalent circle (Fig. 10c). This induction loop can be attributed to the reactions of metal dissolution and formation of corrosion products Mg(OH)$_2$ followed by adsorption of electrolyte ion species. These processes lead to the formation of a cavity-type localised corrosion on the surface [41]. The impedance spectrum of the P-coating fits well with the equivalent circle to Fig. 10d. The Nyquist and Bode-Phase curves of the P-coating indicate that, in addition to two time constants available for the Si-coating, a Warburg element is also present. The presence of the Warburg element in the impedance spectrum indicates that the diffusion control process occurs within the coating. Since the P-coating has a high corrosion rate, to stabilize the dissolution rate of the substrate, rapid penetration of the invading electrolyte into the porous coating/substrate interface is required, which is called corrosion permeation control [15]. In the equivalent circles (Fig. 10), a constant phase element (CPE) is used (instead of an absolute capacitor) to capture the surface heterogeneity factor, resulting in more accurate results by equating the spectra with the electrical equivalent circuit. The capacitance values of the constant phase element are calculated through Eq. 17 [42].
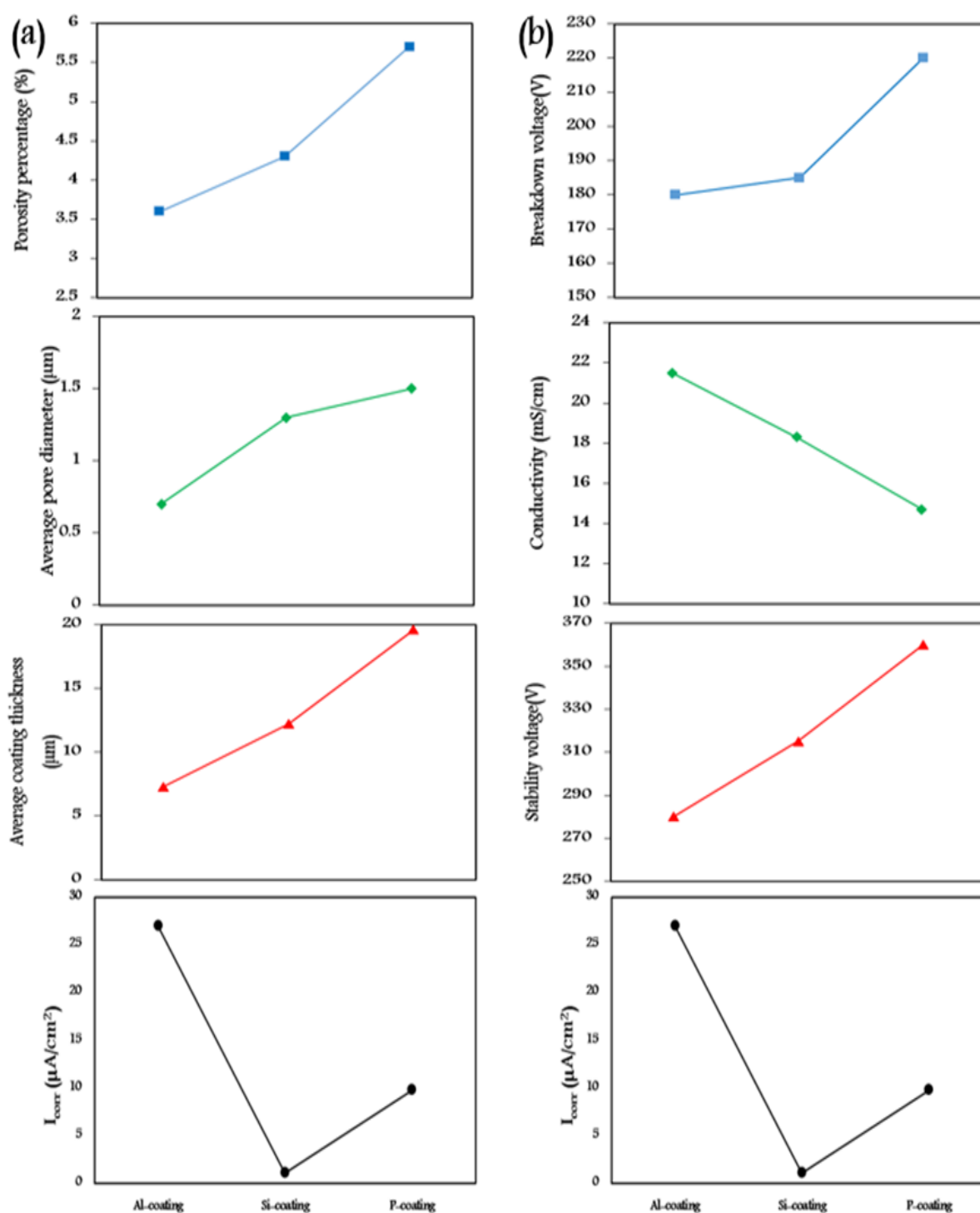
Fig. 7. Correlation of i_{corr} with Morphological characteristics a), electrical process characteristics b) measured for coatings

$$C_{CPE,i} = (Y_{0,i} \cdot R_i^{1-n})^{\frac{1}{n}} \qquad (17)$$

Where $Y_{0,i}$ denotes the admittance constant, R_i represents the parallel resistance to the constant phase element i, and n is the heterogeneity factor. The values of n lie within the range of 0 and 1, indicating that the CPE is absolute resistance

(n= 0) and a capacitor (n= 1), respectively. The results of equating the impedance spectra of the samples with the equivalent electrical circuits are presented in Fig. 10 and Table 7.

The values of R_{coat} and R_{int} of the coatings confirm that the porous layer of the coating cannot provide

significant corrosion resistance, and the overall corrosion resistance of the coating is mainly related to the compacted inner layer. The corrosion resistance of the porous layer (R_{coat}) in the coating is the lowest for the P-coating and the highest for the Al-coating; thus, the resistance of R_{coat} is inversely associated with the degree of porosity of the coating. R_{int} for Si-coating is equal to 17.9 kΩ.cm^2 which is higher than for other samples, possibly due to the presence of a stable forsterite phase in the coating structure, while R_{int}

is equal to 1.2 kΩ.cm^2 for the Al-coating. The physical concept of CPE parameters (n, Y) can justify the dielectric behavior of the electrolyte/ coating interface and the interface of the inner layer/the outer layer [19]. High Y values in the Si-coating may indicate a high level of corrosive electrolyte contact at the interface of the inner layer/the outer layer. On the other hand, the low values of n for this sample may be due to the heterogeneity of the contact surface of the corrosive electrolyte and the coating in their interface.
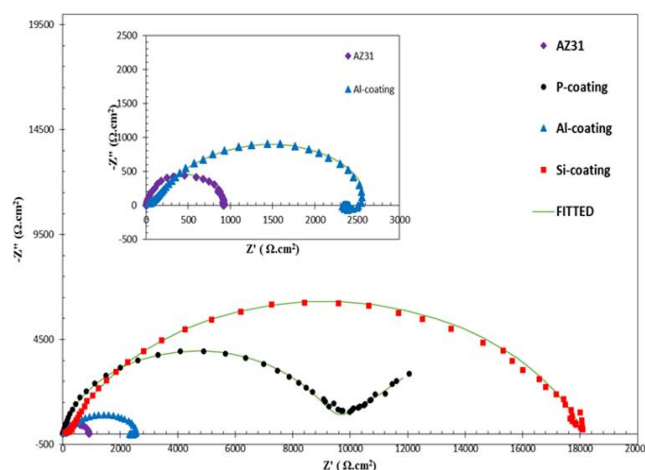

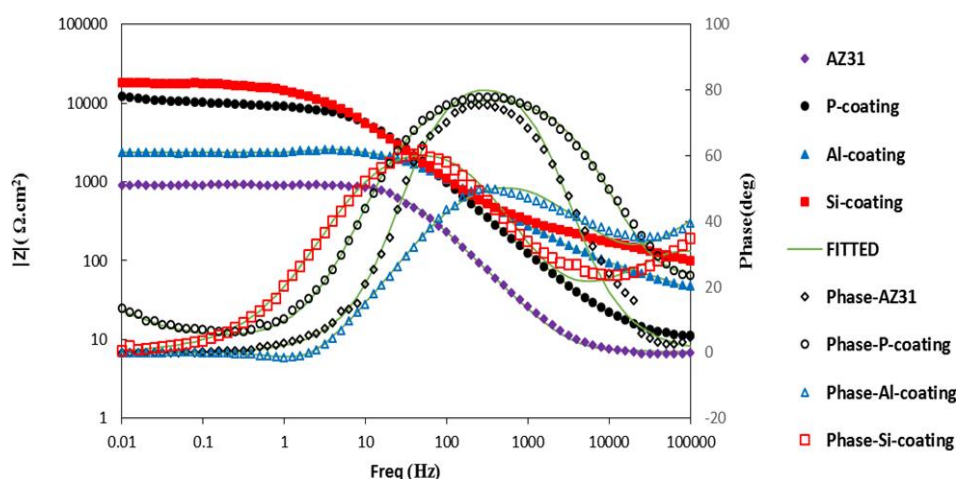**Fig. 8.** Nyquist plots of the PEO coated samples and bare Mg alloy

Fig. 9. Bode-phase plots of the PEO coated and bare Mg alloys

Table 7. Various electrical parameter values obtained after fitting the equivalent circuit to the EIS data

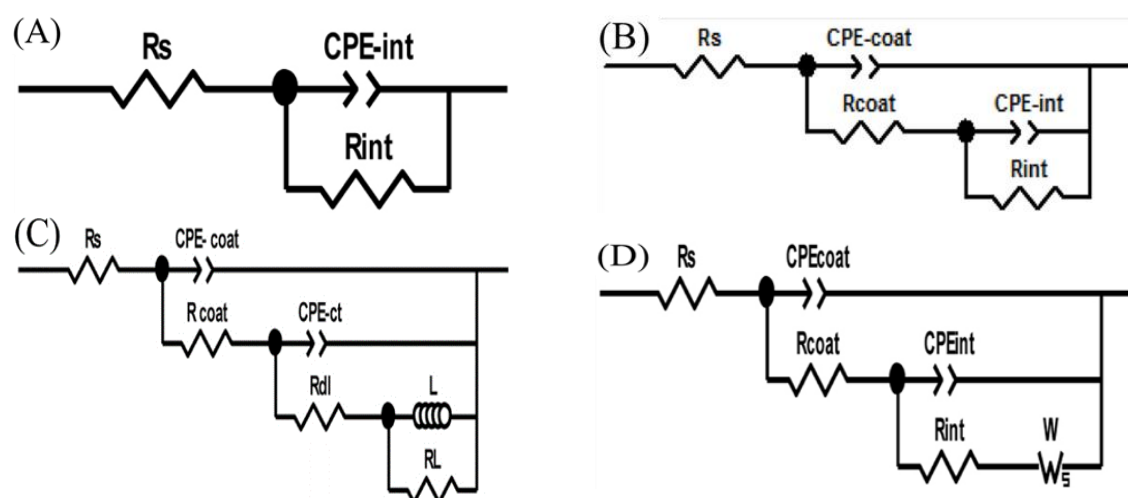| Samples	L (H)	R_L (kΩ.cm^2)	W (Y_0)	R_{int} (kΩ.cm^2)	CPE$_{int}$ Y_{0-int} (Ω^{-1}.cm^{-2}.s^n)	N_{int}	R_{coat} (kΩ.cm^2)	CPE$_{coat}$ Y_{coat} (Ω^{-1}.cm^{-2}.s^n)	N_{coat}	R_s (kΩ.cm^2)	Error of fitting (%)
P-coating	-	-	5.7×10^{-4}	8.9	4.4×10^{-6}	0.89	0.01	3.3×10^{-6}	0.91	0.03	<4.119
Al-coating	50.06	0.9	-	1.2	6.1×10^{-6}	0.7	0.31	1.4×10^{-6}	0.57	0.03	<5.621
Si-coating	-	-	-	17.9	2.4×10^{-6}	0.81	0.22	1.7×10^{-6}	0.67	0.03	<6.427
AZ31	-	-	-	0.9	1.1×10^{-5}	0.96	-	-	-	0.03	<5.173

Fig. 10. Equivalent electrical circuits used for impedance data fitting

Therefore, it can be concluded that the high value of corrosion resistance of the inner layer of Si-coating is due to the high compactness of the phase formed in this coating because the coating has heterogeneous (probably micro-channels that extend from the coating surface to the substrate) that allow penetration of the corrosive electrolyte into the coating.

3.5. Mechanical Properties

Fig. 11 illustrates the engineering tensile stress-strain curves of the samples, which exhibit a significant difference.
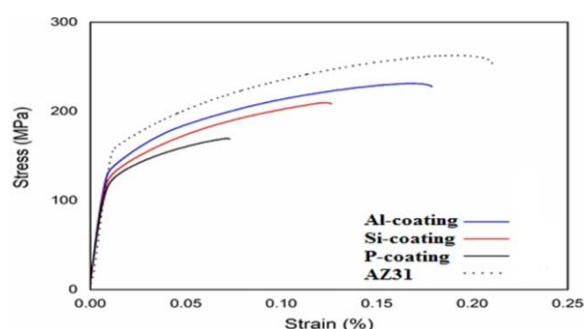

Fig. 11. Stress vs. strain plots of the untreated and PEO-coated AZ31 alloy specimens in air

Two different reasons drove the continuously increasing behavior of curves. Elastic and plastic deformation are present in a tensile test as two general deformation stages. Thus, the information regarding the yield strength (YS) as well as the data associated with plastic deformation (ultimate tensile strength (UTS) and strain (ε)) could be derived from the tensile curves. For the uncoated sample, Hook's law has been ruled in the elastic region, so the tensile stress increased linearly, and the yielding stress (YS) was ~150 MPa at the end of this region. These values have been approximately equal to 133 MPa, 127 MPa, and 120 MPa for Al-coating, Si-coating, and P-coating, respectively (Fig. 12).
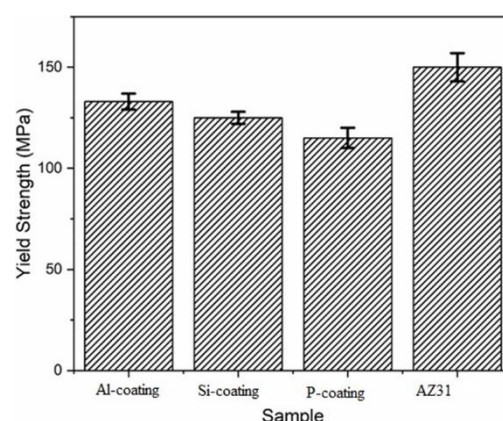

Fig. 12. Yield stress of the untreated and PEO-coated AZ31 alloy specimens in air

In the plastic region, the bare specimen shows the highest UTS (263 MPa) and strain (21%) values. Additionally, it is also found that the coated specimens exhibit lower UTS and strain values as compared to the bare ones. The mechanical properties of the plastic region (UTS and strain) for Al-coating, Si-coating, and P-coating samples are tabulated in Table 8.

The most significant decline was observed in the P-coating, where UTS and strain were reduced by 35% and 66%, respectively. Interestingly, the reduction in YS, UTS, and strain values is inversely related to the average pore diameter and

porosity percentage in the coatings. Accordingly, this drop could be attributed to the presence of the brittle ceramic coating of the PEO specimens [43]. The higher-magnification scanning electron micrograph (Figs. 2 and 3) revealed the presence of cracks and pores in the PEO coating, as well as damaged regions that exposed the substrate (Table 4). During the early stage of the PEO coating process, the establishment of cracks in the inelastic PEO-coated surface and their subsequent development into the substance can be considered a consequence of thermal stress resulting from the rapid solidification of molten oxides in the arc region. Conversely, a rising stress concentration is observed locally and preferentially on the coated samples, which contain numerous pores and cracks, during the tensile test. The latter results in far lower tensile strength and elongation compared to the uncoated one. Indeed, cracks and pores act as stress concentration regions during deformation, so YS, UTS, and strain diminish with the expansion of these areas from the Al-coating to the P-coating. Furthermore, in this elastic stage, the applied deformation was reversible upon the elimination of external stress. However, the coated samples might suffer permanent damage even in this low strain stage [44]. While an external load tensions the specimen during the tensile test, a shear stress will develop at the interface between the coating and the substrate; thus, an induced tensile stress is present within the coating. At adequate loads, when the induced tensile stress outstrips the tensile strength of the coating, it begins to crack. Such separation of the cracks might be caused by periodic sequential cracking of brittle coatings on elastic substrates, as suggested by [18, 45] based on a sinusoidal shear stress distribution model. A similar coating behavior has also been observed through an experiment and reported by Asquith et al. [44] as well as Hiromoto et al. [46].

4. CONCLUSIONS

The effect of an electrolytic solution on the corrosion behaviour and mechanical properties of a coated AZ31 magnesium alloy was characterised via plasma electrolytic oxidation in this study. Based on the experimental results and analyses, several conclusions can be drawn as follows:

- The spark and stability voltage of the PEO process, and as a result, spark characteristics change under the type of electrolyte. With increasing spark and stability voltages, the thickness of the coating and the porosity increased from Al-coating to P-coating due to the intensification of the energy of spark pulses.

- The dominant phase in P-coating and Al-coating was MgO, i.e. Mg_2SiO_4 for Si-coating.

- Investigation of the correlation between the corrosion rate of coatings and the morphological characteristics of the coatings and the electrical characteristics of the process showed that, in addition to the surface quality of the coating, other parameters affect the corrosion resistance of the Si-coating.

- The results of the equilibrium of impedance spectra with suitable equivalent circuits revealed that in the Si-coating, the major portion of the corrosion resistance of the coating was related to the inner layer. The heterogeneity of the interface between the inner and outer layers of the Si-coating resulted in a high amount of corrosive electrolyte contact with the coating. As a result, the high corrosion resistance of the inner layer of the coating is due to its compact, homogeneous structure and stable phase (Mg_2SiO_4) of the inner layer. The tensile strength and elongation diminished from the uncoated to the coated samples.

- Both the tensile strength and elongation dropped by changing the electrolyte from Al-coating to P-coating, while the yield strength was almost similar. The latter could be attributed to the presence of cracks and pores in the brittle PEO ceramic coating, which act as stress concentration regions during deformation, resulting from thermal stress during the coating process and deformation in the elastic stage.

Table 8. Tensile properties of the bare and PEO-coated samples at room temperature

Sample	Ultimate tensile strength (UTS) MPa	Elongation %
Bare	263	21
Al-coating	231	18
Si-coating	209	12.6
P-coating	169	7

REFERENCES

[1] Yu, L., J. Cao, and Y. Cheng, An improvement of the wear and corrosion resistances of AZ31 magnesium alloy by plasma electrolytic oxidation in a silicate–hexametaphosphate electrolyte with the suspension of SiC nanoparticles. Surface and coatings technology, 2015. 276: p. 266-278. https://doi.org/10.1016/j.surfcoat.2015.07.014.

[2] M.S. Jalali, A. Zarei-Hanzaki, Mehdi Malekan, H.R. Abedi, M. Mosayebi, Amir-Reza Kalantari, E. Farabi, Su-Hyeon Kim, Substructure induced dendrite-fragmentation during thermomechanical processing of as-cast Mg-Sn-Li-Zn alloy. Materials Letters, 2021. 305: p. 130690. https://doi.org/10.1016/j.matlet.2021.130690.

[3] Hamdy, A.S., Alkaline-based surface modification prior to ceramic-based cerate conversion coatings for magnesium AZ91D. Electrochemical and solid-state letters, 2007. 10(3): p. C21. https://doi.org/10.1149/1.2430565.

[4] I. Saeki, T. Seguchi, Y. Kourakata, Y. Hayashi, Ni electroplating on AZ91D Mg alloy using alkaline citric acid bath. Electrochimica Acta, 2013. 114: p. 827-831. https://doi.org/10.1016/j.electacta.2013.09.149.

[5] Hsiao, H.-Y., H.-C. Tsung, and W.-T. Tsai, Anodization of AZ91D magnesium alloy in silicate-containing electrolytes. Surface and Coatings Technology, 2005. 199(2-3): p. 127-134. https://doi.org/10.1016/j.surfcoat.2004.12.010.

[6] R. Arrabal, E. Matykina, T. Hashimoto, P. Skeldon, G.E. Thompson, Characterization of AC PEO coatings on magnesium alloys. Surface and coatings technology, 2009. 203(16): p. 2207-2220. https://doi.org/10.1016/j.surfcoat.2009.02.011.

[7] R-G. Hu, S.Zhang, J-F. Bu, C-J. Lin, G-L. Song, Recent progress in corrosion protection of magnesium alloys by organic coatings. Progress in Organic Coatings, 2012. 73(2-3): p. 129-141. https://doi.org/10.1016/j.porgcoat.2011.10.011.

[8] G. Garcés, M.C. Cristina, M. Torralba, P. Adeva, Texture of magnesium alloy films growth by physical vapour deposition (PVD). Journal of alloys and compounds, 2000. 309(1-2): p. 229-238. https://doi.org/10.1016/S0925-8388(00)01075-6.

[9] R.O. Hussein, X. Nie, D.O. Northwood, The application of plasma electrolytic oxidation (PEO) to the production of corrosion resistant coatings on magnesium alloys: a review. Corrosion and Materials, 2013. 38(1): p. 55-65. https://www.researchgate.net/publication/359068870.

[10] A.L. Yerokhin, X. Nie, A. Leyland, A. Matthews, S.J. Dowey, Plasma electrolysis for surface engineering. Surface and coatings technology, 1999. 122(2-3): p. 73-93. https://doi.org/10.1016/S0257-8972(99)00441-7.

[11] Bai, A. and Z.-J. Chen, Effect of electrolyte additives on anti-corrosion ability of micro-arc oxide coatings formed on magnesium alloy AZ91D. Surface and Coatings Technology, 2009. 203(14): p. 1956-1963. https://doi.org/10.1016/j.surfcoat.2009.01.032.

[12] R.F. Zhang, D.Y. Shan, R.S. Chen, E.H. Han., Effects of electric parameters on properties of anodic coatings formed on magnesium alloys. Materials Chemistry and Physics, 2008. 107(2-3): p. 356-363. https://doi.org/10.1016/j.matchemphys.2007.07.027.

[13] T. Mi, B. Jiang, Z. Liu, L. Fan., Plasma formation mechanism of microarc oxidation. Electrochimica Acta, 2014. 123: p. 369-377. https://doi.org/10.1016/j.electacta.2014.01.047.

[14] R.O. Hussein, X. Nie, D.O. Northwood, An investigation of ceramic coating growth mechanisms in plasma electrolytic oxidation (PEO) processing. Electrochimica Acta, 2013. 112: p. 111-119. https://doi.org/10.1016/j.electacta.2013.08.137.

[15] A. Ghasemi, V.S. Raja, C. Blawert, W. Dietzel, K.U. Kainer, The role of anions in the formation and corrosion resistance of the plasma electrolytic oxidation coatings. Surface and Coatings Technology, 2010. 204(9-10): p. 1469-1478. https://doi.org/10.1016/j.surfcoat.2009.09.069.

[16] Z.U. Rehman, B-H. Ahn, Y. S. Jeong, J-I.Song, and B-H. Koo, The influence of various additives on the properties of PEO coatings formed on AZ31 Mg alloy. Surface Review and Letters, 2016. 23(03):

p. 1650006. https://doi.org/10.1142/S021 8625X16500062.

[17] Srinivasan, P.B., C. Blawert, and W. Dietzel, Effect of plasma electrolytic oxidation coating on the stress corrosion cracking behaviour of wrought AZ61 magnesium alloy. Corrosion science, 2008. 50(8): p. 2415-2418. https://doi.org/10.1016/j.corsci.2008.05.018.

[18] Gao, Y., A. Yerokhin, and A. Matthews, Mechanical behaviour of cp-magnesium with duplex hydroxyapatite and PEO. https://doi.org/10.1016/j.msec.2014.12.081.

[19] T. Zehra, S. A. Patil, N. K. Shrestha, A.Fattah-alhosseini, M. Kaseem, Anionic assisted incorporation of WO3 nano-particles for enhanced electrochemical properties of AZ31 Mg alloy coated via plasma electrolytic oxidation. Journal of Alloys and Compounds, 2022: p. 165445. https://doi.org/10.1016/j.jallcom.2022.165445.

[20] Bahramian, A., K. Raeissi, and A. Hakimizad, An investigation of the characteristics of Al_2O_3/TiO_2 PEO nanocomposite coating. Applied Surface Science, 2015. 351: p. 13-26. https://doi.org/10.1016/j.apsusc.2015.05.107.

[21] Venkateswarlu K., Rameshbabu N., Sreekanth D., Bose A.C., Muthupandi V., Babu N.K., Subramanian S, Role of electrolyte additives on in-vitro electrochemical behavior of micro arc oxidized titania films on Cp Ti. Applied Surface Science, 2012. 258(18): p. 6853-6863. https://doi.org/10.1016/j.apsusc.2012.03.118.

[22] Albella, J., I. Montero, and J. Martinez-Duart, A theory of avalanche breakdown during anodic oxidation. Electrochimica Acta, 1987. 32(2): p. 255-258. https://doi.org/10.1016/0013-4686(87)85032-6.

[23] Ikonopisov, S., Theory of electrical break-down during formation of barrier anodic films. Electrochimica Acta, 1977. 22(10): p. 1077-1082. https://doi.org/10.1016/0013-4686(77)80042-X.

[24] S. Stojadinović, R. Vasilić, M. Petković, B. Kasalica, I. Belča, A. Žekić, Lj. Zeković., Characterization of the plasma electrolytic oxidation of titanium in sodium metasilicate. Applied Surface Science, 2013. 265: p. 226-233. https://doi.org/10.1016/j.apsusc.2012.10.183.

[25] Raj, V. and M.M. Ali, Formation of ceramic alumina nanocomposite coatings on aluminium for enhanced corrosion resistance. Journal of Materials Processing Technology, 2009. 209(12-13): p. 5341-5352. https://doi.org/10.1016/j.jmatprotec.2009.04.004.

[26] P. Bala Srinivasan, J. Liang, C. Blawert, M. Störmer, W. Dietzel, Effect of current density on the microstructure and corrosion behaviour of plasma electrolytic oxidation treated AM50 magnesium alloy. Applied Surface Science, 2009. 255(7): p. 4212-4218. https://doi.org/10.1016/j.apsusc.2008.11.008.

[27] Jiang, B. and Y. Wang, Plasma electrolytic oxidation treatment of aluminium and titanium alloys, in Surface engineering of light alloys. 2010, Elsevier. p. 110-154. https://doi.org/10.1533/9781845699451.2.110.

[28] Lou, B.-S., et al., Effects of processing parameters on the adhesion and corrosion resistance of oxide coatings grown by plasma electrolytic oxidation on AZ31 magnesium alloys. Journal of Materials Research and Technology, 2021. 10: p. 1355-1371. https://doi.org/10.1016/j.jmrt.2020.12.108.

[29] Bih-Show Lou, Chien-An Yen, Yen-Yu Chen, Jyh-Wei Lee, Analysis on the micro-structure of ceramic coating layer fabricated by plasma electrolytic oxidation. In Materials science forum. 2007. Trans Tech Publ. https://doi.org/10.1016/j.jmrt.2020.12.108.

[30] Sreekanth, D., N. Rameshbabu, and K. Venkateswarlu, Effect of various additives on morphology and corrosion behavior of ceramic coatings developed on AZ31 magnesium alloy by plasma electrolytic oxidation. Ceramics International, 2012. 38(6): p. 4607-4615. https://doi.org/10.1016/j.ceramint.2012.02.040.

[31] S.V. Gnedenkov, O.A. Khrisanfova, A.G. Zavidnaya, S.L. Sinebryukhov, V.S. Egorkin, M.V. Nistratova, A. Yerokhin, A. Matthew, PEO coatings obtained on an Mg–Mn type alloy under unipolar and bipolar modes in silicate-containing electrolytes. Surface and Coatings Technology, 2010. 204(14): p. 2316-2322. https://doi.org/10.1016/j.surfcoat.2009.12.024

[32] Shi-Gang Xin, Li-Xin Song, Rong-Gen Zhao, Xing-Fang Hu, Composition and

thermal properties of the coating containing mullite and alumina. Materials Chemistry and Physics, 2006. 97(1): p. 132-136. https://doi.org/10.1016/j.matchemphys.2005.07.073.

[33] Durdu, S. and M. Usta, Characterization and mechanical properties of coatings on magnesium by micro arc oxidation. Applied Surface Science, 2012. 261: p. 774-782. https://doi.org/10.1016/j.apsusc.2012.08.099.

[34] Fattah-alhosseini, A., R. Chaharmahali, and K. Babaei, Effect of particles addition to solution of plasma electrolytic oxidation (PEO) on the properties of PEO coatings formed on magnesium and its alloys: A review. Journal of Magnesium and Alloys, 2020. 8(3): p. 799-818. https://doi.org/10.1016/j.jma.2020.05.001.

[35] Stern, M. and A. Geary, A theoretical analysis of the shape of polarization curves. J. Electrochem. Soc, 1957. 104(1): p. 56-63. https://doi.org/10.1149/1.2428473.

[36] J.L. Xu, S.C. Tao, L.Z. Bao, J.M. Luo, Y.F. Zheng, Effects of Mo contents on the microstructure, properties and cytocompatibility of the microwave sintered porous Ti-Mo alloys. Materials Science and Engineering: C, 2019. 97: p. 156-165. https://doi.org/10.1016/j.msec.2018.12.028.

[37] Sarbishei, S., M.A.F. Sani, and M.R. Mohammadi, Study plasma electrolytic oxidation process and characterization of coatings formed in an alumina nanoparticle suspension. Vacuum, 2014. 108: p. 12-19. https://doi.org/10.1016/j.vacuum.2014.05.008.

[38] Xiaoting Shi, Yu Wang, Hongyu Li, Shufang Zhang, Rongfang Zhao, Guoqiang Li, Rongfa Zhang, Yang Sheng, Siyue Cao, Youjun Zhao, Linna Xu, Ying Zhao, Corrosion resistance and biocompatibility of calcium-containing coatings developed in near-neutral solutions containing phytic acid and phosphoric acid on AZ31B alloy. Journal of Alloys and Compounds, 2020. 823: p. 153721. https://doi.org/10.1016/j.jallcom.2020.153721.

[39] J. Liang, P. Bala Srinivasan, C. Blawert, M. Störmer, W. Dietzel, Electrochemical corrosion behaviour of plasma electrolytic oxidation coatings on AM50 magnesium alloy formed in silicate and phosphate based electrolytes. Electrochimica Acta, 2009. 54(14): p. 3842-3850. https://doi.org/10.1016/j.electacta.2009.02.004.

[40] Xiaopeng Lu, Carsten Blawert, Yuanding Huang, Henry Ovri, Mikhail L. Zheludkevich, Karl Ulrich Kainer, Plasma electrolytic oxidation coatings on Mg alloy with addition of SiO2 particles. Electrochimica Acta, 2016. 187: p. 20-33. https://doi.org/10.1016/j.electacta.2015.11.033.

[41] Hongping Duan, Keqin Du, Chuanwei Yan, Fuhui Wang, Electrochemical corrosion behavior of composite coatings of sealed MAO film on magnesium alloy AZ91D. Electrochimica Acta, 2006. 51(14): p. 2898-2908. https://doi.org/10.1016/j.electacta.2005.08.026.

[42] Rassouli, L., R. Naderi, and M. Mahdavain, The role of micro/nano zeolites doped with zinc cations in the active protection of epoxy ester coating. Applied Surface Science, 2017. 423: p. 571-583. https://doi.org/10.1016/j.apsusc.2017.06.245.

[43] P. Bala Srinivasan, C. Blawert, W. Dietzel, K.U. Kainer, Stress corrosion cracking behaviour of a surface-modified magnesium alloy. Scripta Materialia, 2008. 59(1): p. 43-46. https://doi.org/10.1016/j.scriptamat.2008.02.032.

[44] Asquith, D., et al. Measurement of the interfacial shear strength of a PEO coated aluminium alloy. In Proceedings of the 17th European Conference on Fracture, Brno, Czech Republic. 2008.

[45] Agrawal, D.C. and R. Raj, Measurement of the ultimate shear strength of a metal-ceramic interface. Acta Metallurgica, 1989. 37(4): p. 1265-1270. https://doi.org/10.1016/0001-6160(89)90120-X.

[46] Hiromoto, S., M. Tomozawa, and N. Maruyama, Fatigue property of a bioabsorbable magnesium alloy with a hydroxyapatite coating formed by a chemical solution deposition. Journal of the mechanical behavior of biomedical materials, 2013. 25: p. 1-10. https://doi.org/10.1016/j.jmbbm.2013.04.021.

Nomenclature	
PEO	Plasma Electrolyte Oxidation
Si-coating	Silicate-containing sample
P-coating	Polyphosphate-containing sample
Al-coating	Aluminate-containing sample
SEM	Scanning Electron Microscopy
PVD	physical vapor deposition
EDX	Energy Dispersive x-ray Spectroscopy
XRD	X-Ray Diffraction
DC	Direct Current
SCE	Saturated Calomel Electrode
FRA	frequency response analyzer
V_{BD}	Breakdown Voltage
a_B	definite constant for the metal
b_B	definite constant for the electrolyte
k	ionic conductivity of the electrolyte
E_P	single pulse energy
U_P	pulse voltage
I_p	pulse current
t_{on}	pulse-on time
OCP	Open Circuit Potential
i_{corr}	corrosion current density
E_{corr}	corrosion potential
β_c	cathodic Tafel slopes
β_a	anodic Tafel slopes
ASTM	American Standard Test Method
R_P	Polarization Resistance
CPE	Constant Phase Element
$C_{CPE,i}$	capacitance values of the constant phase element
$Y_{0,i}$	admittance constant
R_i	parallel resistance to the constant phase element I
n	heterogeneity factor.
YS	Yield Strength
UTS	Ultimate Tensile Strength
ε	Strain

100